Source Parameterization of Finite Faults in Earthquake Ground Motion Simulation

Ameneh HoushmandViki[1] and Anoushiravan Ansari[2]*

1. Ph.D. Student, Geophysics, International Institute of Earthquake Engineering and Seismology (IIEES), Tehran, Iran
2. Associate Professor, Seismological Research Center, International Institute of Earthquake Engineering and Seismology, Tehran, Iran, * Corresponding Author; email: a.ansari@iiees.ac.ir

Received: 18/12/2017
Accepted: 11/04/2018

ABSTRACT

The effect of interpolation function for describing spatial variations of slip on the fault surface is investigated using finite fault simulation. In analogy with h-p notion in finite element method, the effect of increasing the order of interpolation function and decreasing the size of elements is studied here. In this regard, the fault surface is discretized using different elements, namely, constant discontinuous elements with various sizes, and first order contentious elements with different sizes. In order of parameterization, a bilinear interpolation technique is introduced to represent variation of source parameters within the subfault area. To provide an objective basis for comparison, the September 28, 2004 Parkfield earthquake M_w 6.1 is considered and time-frequency, envelope-phase goodness-of-fit criteria is calculated to compare synthetic and observed waveforms quantitatively in time and frequency domains. It was revealed that by increasing the order of interpolation function, the overall consistency of observed and synthetic waveforms will increase, while the expense of computational analyses will also increase accordingly.

Keywords:
Interpolation, h-p notion, Parkfield earthquake, Goodness-of- fit, Finite fault simulation

1. Introduction

Simulation of earthquake ground motion has a profound implications for seismological and engineering applications. From a seismological point of view, forward modeling provides bases for solving inverse problems and obtaining the rupture process of the fault surface based on observed records of the earthquake. More specifically, in non-linear inverse problems, the procedure to obtain a solution is based on solving a large number of forward problems. By comparing synthetic and observed records, it is possible to obtain the history of the development of the rupture and the time function describing the slip on the fault. From engineering point of view, ground motion simulation provides means to assess the ground shaking level at different points on the earth surface. Traditionally, ground motion records of past earthquakes are used as representative of ground shaking in engineering design applications. Unfortunately, the library of existing recordings only samples a small subset of possible earthquake scenarios. In this condition, ground motion simulation has made prospects to access ground-motion synthesis for upcoming earthquakes.

Earthquake rupture can be approached in two different ways known as kinematic and dynamic. Kinematic models of the source consider the slip of the fault without relating it to stresses cause it. The second approach considers the complete fracture process relating the fault slip to the stress acting on the fault region. Kinematic earthquake rupture is described purely in terms of the slip vector as a

function of the coordinates on the fault plane and time. In this type of model, it is relatively simple to determine the corresponding elastic displacement field [1].

Considering kinematic source models, the process of numerically simulating the strong-motion time series dates back to the work of Hartzell [2] and Irikura [3]. The simulation techniques are extended to include the stochastic representation of source and path effects [4], theoretical full waveform Green's functions [5] or various combinations of these approaches. A comprehensive comparison of many kinematic simulation approaches was provided by Hartzell et al. [6]. For simulation of earthquake ground motion by hybrid methods, it is a common task to discriminate between high and low frequency components of motion around 1 Hz. The low frequency component of motion is usually modeled through the deterministic method that contains a theoretically rigorous representation of fault rupture and wave propagation effects. High frequency components of motion are commonly calculated by stochastic models basically because of the random nature of high frequency components of motion.

In kinematic simulation approach, the fault surface is divided into some small subfaults. The value of slip is usually considered to be uniform among the surface of each subfault along strike and dip directions. Similarly, other rupture parameters including rise time and rake angle, are also considered to be constant among each subfault. The assumption of constant values of kinematic parameters comes from the need of parameterization and discretization of the fault surface in representation theory [7]. However, it is possible to use higher order interpolation function to model variability of slip and other parameters among each subfault. Liu and Archuleta [8] introduced the linear interpolation function to model surface variability of slip among subfaults in the inversion of 1989 Loma Prieta earthquake. Custodio [9] also used the linear interpolation method for finite fault inversion of 2004 Parkfield earthquake.

Increasing the order of interpolation will result in higher computational demand [10], both for solving the forward and inverse problems. However, there is a question that how much the accuracy of simulation will be improved by increasing the order of interpolation while a considerable increase in computational time is taken into account. This paper pursues to answer this question. In this regard, in the first section, the principles of kinematic simulation of earthquake will be reviewed. It will be followed by the description of fault discretization containing elements with the order of zero (constant) and one (linear). To examine the influence of increasing the order of interpolation in discretization process of fault surface, the case of September 28, 2004 M_w 6.1 Parkfield earthquake is considered because of the comprehensive recordings of this event. At the end, a discussion is provided regarding the trade-off between the increase in simulation accuracy and the computational effort of analyses.

2. Principle of Deterministic Simulation of Earthquakes

Faulting is characterized by the slipping of one side of a fault surface with respect to the other. The process of slip on a buried fault and the waves radiated from it can naturally be analyzed by the representation theorem. If the earth is modeled as an elastic solid, then the displacement field due to a point unit dislocation can be taken as a Green's function for the earthquake faulting problem. The displacement field at all points in the earth due to an arbitrary distribution of slip on a fault is expressed as an integral over the fault surface of the slip distribution convolved with the Green's function, as follow [7]:

$$u_i(x,t) = \int_{-\infty}^{+\infty} d\tau \iint \left[u_j(\varepsilon,\tau)\right] C_{jkpq} G_{ip,q}(x,t,\varepsilon,\tau)\, v_k\, d \qquad (1)$$

where $u_i(x,t)$ is the displacement field in (x,t), S is the fault plane, C_{jkpq} are elastic constants, G is the Green's function of the medium and $[u]$ is the dislocation field on the fault plane. The representation theorem provides an expression for the radiation in an elastic media resulting from the creation of a discontinuity in the displacement and stress fields across a fault surface. The Green's function, G, used in the representation theorem is the response of the medium to a unit point force in the absence of discontinuities. The Green's function can be used to satisfy any boundary condition on the fault surface;

hence, the elastodynamic equations only need to be solved once.

3. Discretization of Fault Surface

In order to solve the forward or inverse problem, it is necessary to obtain the discrete form of surface integral in Equation (1). In this regard, the fault surface is divided into discrete subfaults. Each subfault is characterized by the value of slip along strike and dip angles, rise time and rupture time. Olson and Apsel [11] provided a method to estimate the surface integral with constant elements where locations within each element were assumed to undergo the same slip within a specified time shift. Taking the assumption of constant slip among each subfault, the slip function on the fault surface can be written as [11]:

$$s(x,t)=\sum_{j=1}^{J}X_j(x)s_jP_j(x,t)$$

$$X_j(x)=\begin{cases}1 & \text{if } X \text{ in } j^{th} \text{ subfault}\\ 0 & \text{else}\end{cases} \quad (2)$$

where J is the total number of subfaults, s_j is the slip value of subfault j and $P_j(x, t)$ is the time dependence of slip in j^{th} subfault. $P_j(x, t)$ represents the combination of rupture time and rise time of slip in subfault j. Substituting Equation (2) in Equation (1), we have:

$$u_i(x,t)=\sum_{j=1}^{J}s_j.g_j^i(x,t).a_j \quad (3)$$

where $g_j^i(x,t)$ is the Green's function for the j^{th} cell at position x in the i^{th} component direction convolved with s_j and a_j where a_j is the area of the subfault. It is possible to write Equation (3) in a matrix form and solve forward or inverse problems accordingly.

Liu and Archuleta [8] used the linear interpolation function to model the variability of simulation parameters within each subfault. In this approach, the subfaults are quadrilateral elements which should not necessarily be rectangular and equal in area. The shape and area of each quadrilateral can differ from others [8]. It is assumed that the subfault is a quadrilateral element defined by the location of four nodal points. If the quadrilateral element is rectangular then the bilinear interpolation can be directly applied. Rectangular elements are convenient

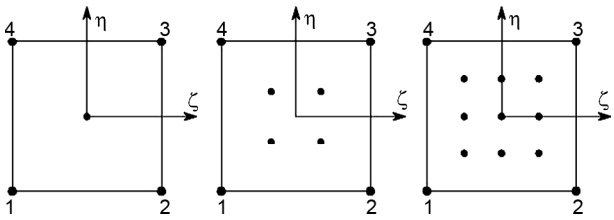

Figure 1. Four-node rectangle scheme in a 2D domain considering one integration point (left), four integration points (middle), and nine integration points (right).

to use in modeling regular geometries. The simplest of the rectangular family of elements is the four-node rectangle, where it is assumed that the sides of the rectangular are parallel to the global Cartesian axes. By convention, we number the nodes sequentially in a counterclockwise direction (Figure 1).

Assuming the linear variation of parameters inside each rectangular element, the coordinates of any arbitrary point inside the element can be represented as:

$$x^e(\xi,\eta)=\sum_{i=1}^{4}N_i(\xi,\eta)x_i^e$$

$$y^e(\xi,\eta)=\sum_{i=1}^{4}N_i(\xi,\eta)y_i^e \quad (4)$$

where ξ, η are local coordinates in a bi-unit square, e is the index of the subfault and N_i is the shape function of linear interpolation defined as:

$$N_1(\xi,\eta)=\frac{1}{4}(1-\xi)(1-\eta)$$

$$N_2(\xi,\eta)=\frac{1}{4}(1+\xi)(1-\eta)$$

$$N_3(\xi,\eta)=\frac{1}{4}(1+\xi)(1+\eta) \quad (5)$$

$$N_4(\xi,\eta)=\frac{1}{4}(1-\xi)(1+\eta)$$

Similarly, any simulation parameters inside the element can be obtained by linear interpolation of nodal values of elements as:

$$m^e(\xi,\eta)=\sum_{i=1}^{4}N_i(\xi,\eta)m_i^e \quad (6)$$

where $m^e(\xi,\eta)$ could be any simulation parameters including the slip value, rake angle, rupture velocity and rise time. Inside each element or subfault, it is possible to simulate the waveform radiated from rupture by a series of point dislocations that cover the fault. In this regard, $N\xi$ points along strike and

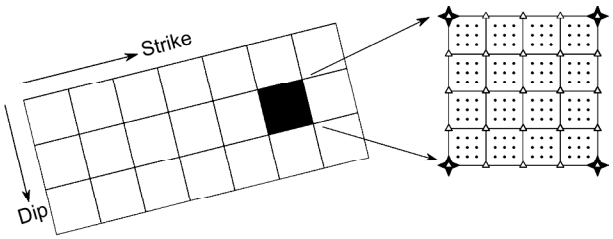

Figure 2. Discretization of the fault surface and subfaults. Reproduced by the slip model of Custodio et al. [12].

$N\eta$ points along dip are assigned inside each element with equal distance with each other. Indeed, to calculate the surface integral of Equation (1), each element contains $N\xi$ $N\eta$ interior point sources along strike and dip angles respectively. Figure (2) depicts the discretization of fault surface and subfaults. In forward problem, the source parameters are known on nodal points (black stars). The Green's function are also evaluated inside each subfault on the points shown with white triangles. The surface integration of Equation (1) is evaluated on black dots. The source parameters and Green's functions are evaluated for each integration point (black dots) using the bilinear interpolation relationship of Equations (6). Taking this discretization procedure, the Equation (1) could be written as a similar form as Equation (3), while J is representing the total number of integration points (black dots in Figure 2).

If we assume that all elements or subfaults have rectangular shape, the local coordinate (ξ, η) inside each subfault is:

$$\xi_j = \frac{2j-1}{N\xi} - 1 \qquad j = 1 \cdots N\xi$$
$$\eta_k = \frac{2k-1}{N\eta} - 1 \qquad k = 1 \cdots N\eta \tag{7}$$

Using this procedure, the source parameters have continuous variation within the whole fault, although their values are not smooth at the nodal points. Moreover, the radiated wave from each subfault is dependent on the source parameters of four nodes of each subfault, rather than only one parameter in the case of constant elements. As Liu and Archuleta [8] noticed, since each node connects four adjacent elements to each other, the bilinear interpolation enforces a spatial correlation among source parameters in finite fault modeling. The similar formulation could also be applied for higher order interpolation functions. The only difference is in Equation (5) where the appropriate form of shape functions shall be used for each kind of interpolation function.

In the following section, the simulation analyses will be performed for the 2004 M_w 6.1 Parkfield earthquake with constant and linear elements.

4. Simulation Analysis

In this section, the effect of using different interpolation functions to describe the variability of simulation parameters is investigated by solving a number of forward problems. In discretization of fault surface, apart from the order of interpolation function, the size of elements is an important parameter. Generally, it is possible to increase the accuracy of interpolation either by refining the subfaults or by increasing the order of interpolation functions with fixed subfault size [13]. It is also possible to combine two approaches by refining the element size and increasing the order of interpolation function. An obvious question that arises is how well these methods compare with the traditional constant elements for the evaluation of integral Equation (1). In the case of finite element method (FEM), the capability of increasing the order of interpolation function is coupled with mesh refinement (the *h -p*, FEM) and leads to exponential rates of convergence [14]. However, in the case of integral equation of Equation (1), the answer to the question shall be investigated by using different interpolation schemes to simulate a unique earthquake and compare the simulated waveforms with observed time histories in order to have an objective criteria for discussion. Thus, it is necessary to choose a well-recorded and well-documented earthquake with sufficient number of recordings to provide a statistical meaningful experiment. The September 28, 2004 M_w 6.1 Parkfield earthquake is an event that satisfies all these conditions. This earthquake provided one of the largest amounts of near-source strong ground motion records with more than 40 recording stations in an epicentral distance less than 32 km [9].

To make an objective comparison between observed and simulated time histories, Kristekova et al. (2006) provided a goodness-of-fit criteria by making Time-Frequency (TF) comparison between

waveforms. Following, the goodness-of-fits criteria of Kristekova et al. [15] has been reviewed and a brief description of M_w 6.1 Parkfield earthquake has been provided. Later, a number of analyses have been performed to make a comparison between the results of simulation with different interpolation schemes.

4.1. TF Goodness-of-Fit Criteria for Quantitative Comparison of Time Signals

It is often necessary to compare two signals whose envelopes-phase differ considerably. Such comparison usually forms bases to quantify the validity of new theoretical models or methods of analyses. Kristekova et al. [15] provided an extension of TF misfit criteria for quantitative and objective comparison of observed and synthetic time signals. The TF representation makes it possible to study a spectral content at any time, as well as a time history at any frequency. To make the comparison between two signals, Kristekova et al. [16] introduced a method for comparing the envelopes of TF representation of two signals as well as their corresponding phases. Having the envelope and phase differences at a given TF point, they introduced a normalized TF misfit criteria that ranges between zero for least similarity and 10 for the most agreement between two signals. Figure (3) depicts the numerical values of goodness-of-fit criteria in addition to verbal classification for the overall comparison of signals.

Anderson [17] also provided another goodness-of-fit criteria mainly based on characteristics relevant in the earthquake-engineering applications.

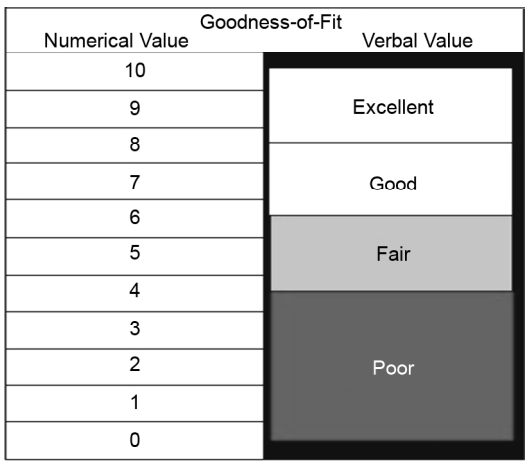

Figure 3. Discrete goodness-of-fit numerical and verbal values.

He filtered the signals into narrow frequency subintervals and then made comparison between some engineering characteristics of the signals, namely, peak acceleration, peak velocity, peak displacement, Arias intensity, the integral of velocity squared, Fourier spectrum and acceleration response spectrum, the shape of the normalized integrals of acceleration and velocity squared, and the cross correlation. He assigned a 10-level score to each characteristic parameter, as 10 points for the most agreement.

Although the Anderson's goodness-of-fit criteria is more tangible from engineering point of view, but the envelope-phase misfits are mostly useful for comparing relatively close envelopes-phases in simulation process, specially where there are too much simulated waveforms to present. The framework proposed by Kristekova et al. [15] is more robust and objective from mathematical and signal processing point of view. Kristekova et al. [15] criteria is used in this study to make a comparison between observed and simulated time histories.

4.2. An Overview of 2004 M_w 6.1 Parkfield Earthquake and Modeling Parameters

An earthquake with M_w 6.1 struck the central coast of California in the Parkfield region at 17:15:24 (UTC), on September 28, 2004. The epicenter was 11 km south-east of Parkfield, at a depth of approximately 8 km. U.S. Geological Survey (USGS) indicates that the event had a strike-slip mechanism. The 2004 Parkfield earthquake ruptured an opposite direction along the same section of the San Andreas Fault with similar magnitude to the 1966 Parkfield earthquake [9]. Strong motions of the 2004 earthquake have been recorded by California Geological Survey (CGS) and USGS instruments.

To infer the kinematic finite-fault nature of 2004 M_w 6.1 Parkfield earthquake, Custodio et al. [12], applied a non-linear global inversion on different data subsets of near-source ground motion measurements and got a slip model with amplitudes less than 0.65 m surrounding two major areas on the fault surface (Figure 4a). Ji [18] determined a heterogeneous slip distribution by the low-frequency waveform inversion and identified two specific patches (Figure 4b). Dreger et al. [19], depicted a 2D source model on the incorporating near-field

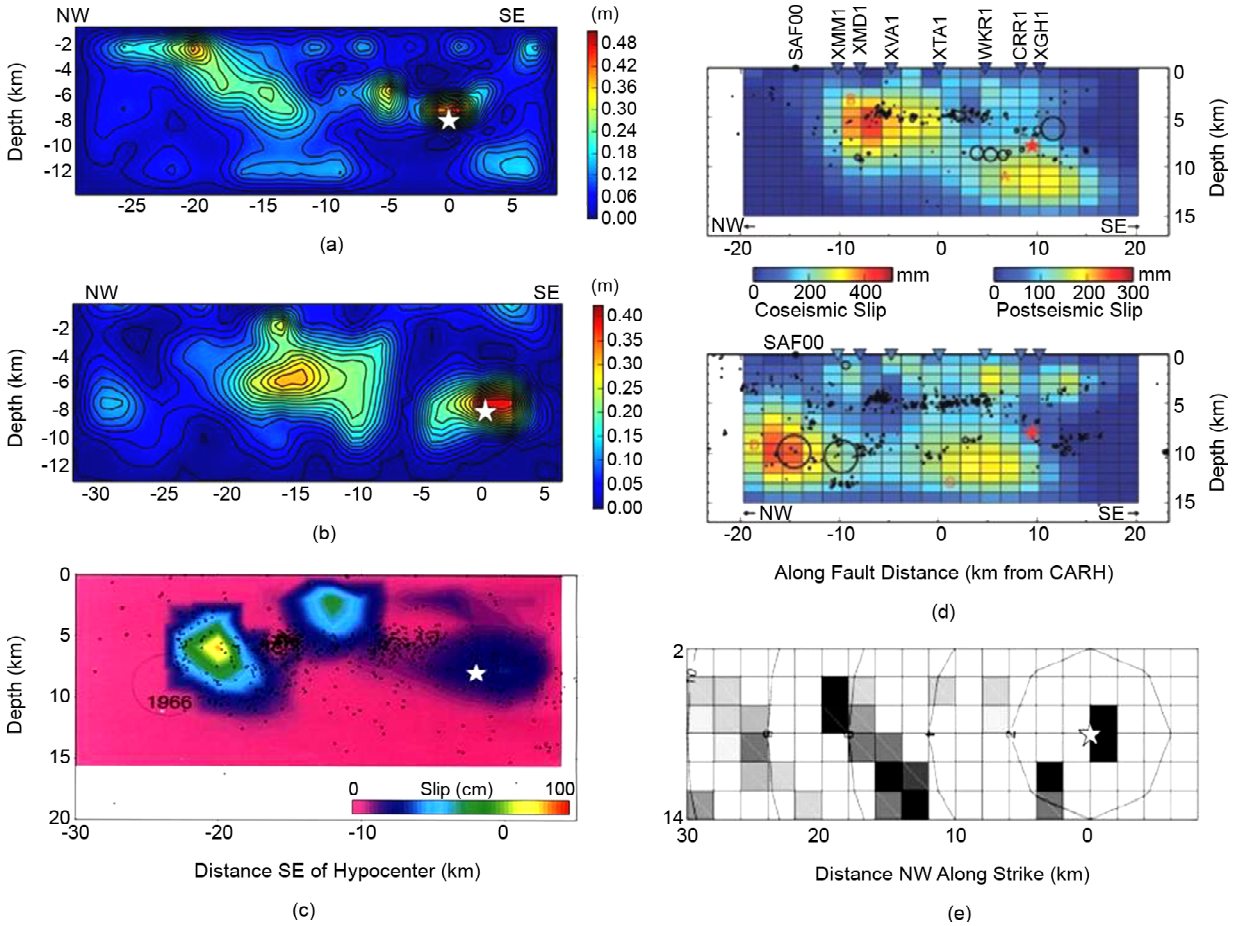

Figure 4. a) Custodio et al. [12] slip model, b) Ji [18] slip model, c) Dreger et al. [19] slip model, d) Johanson et al. [20] slip model, e) Mendoza and Hartzell [21] slip model.

records of a GPS array and resulted a line-source model consistent with the distribution of 39 aftershocks occurred 48 hours after the event (Figure 4c). InSAR and GPS data for coseismic and postseismic patterns were inverted by Johanson et al. [20], simultaneously. On the coseismic slip model, two asperities occur with the larger being at the northwest of the hypocenter by 15 km, and for the postseismic period the model identifies a deep slip patch (Figure 4d). Mendoza and Hartzell [21], determined the coseismic slip using both numerically calculated synthetic Green's function based on a flat-layered 1D velocity model and EGF's derived from a M_w 5.0 aftershock (Figure 4e). The results show that the slip expands to the northwest increasing the rupture velocity. The source model inferred using synthetic Green's function is consistent with the source model obtained by Custodio et al. [12]. Barnahart and Lohman [22], Houlie et al. [23] and also many others have discussed about the rupture model of 2004 M_w 6.1 Parkfield earthquake.

In this study, the source model of 2004 M_w 6.1 Parkfield earthquake is used for solving a number of forward problems and make a comparison between synthetic time histories and strong motion records of this event. A strike-slip fault is considered with 140 degrees strike, 87 degrees dip and 40 km length [24]. Indeed, strong motion records reported by 26 CGS stations around the epicenter at a great azimuthal coverage are used in this study (Figure 5). In the calculation procedure, we consider the Custodio et al. [12] slip model (http://equake-rc.info/srcmod, Figure 6). The epicenter is located at 35.81 latitudes and -120.37 longitudes [24]. In simulation analyses, the velocity waveforms are considered for comparison and all waveforms and Green's functions are filtered by a 4th order Butterworth band-pass filter with linear phase response in 0.16-1.00 Hz frequency range.

To compute the synthetic seismograms for each station, the Green's functions should be calculated at any point on the fault area and then convolve them with the specific source parameters at that point.

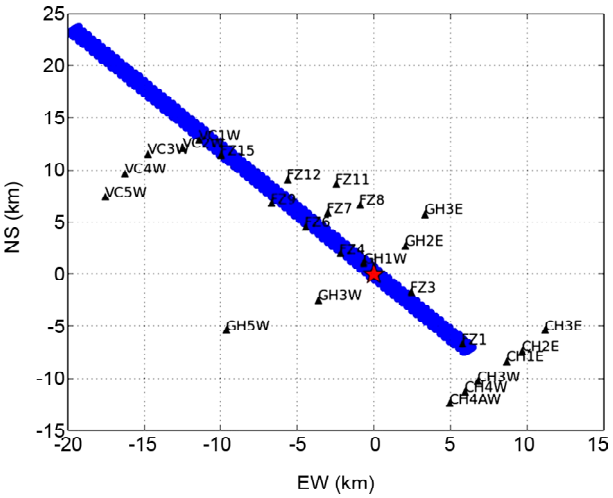

Figure 5. Location of the 2004 Mw 6.1 Parkfield earthquake and 26 stations used in this study. Epicenter is shown with a red star.

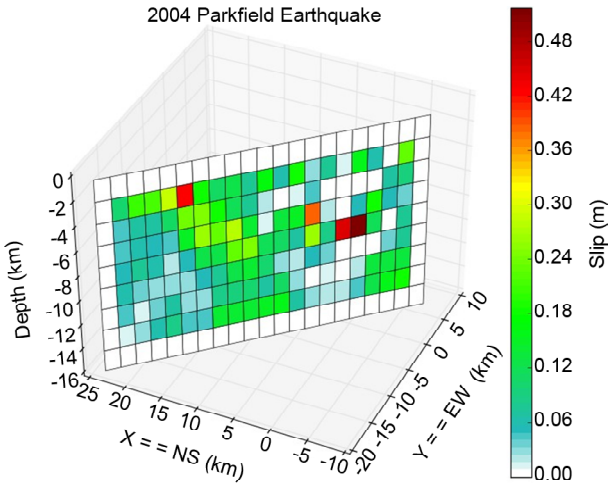

Figure 6. 2004 M_w 6.1 Parkfield slip model (http://equake-rc.info/srcmod).

The Green's functions are computed by AXITRA code [25], [26] using the frequency-wavenumber method of Bouchon [27]. The 1D velocity structure is used in the computation of Green's functions. The P-wave structure is obtained by interpolation of the 3D model [23]. The S-wave structure is obtained by applying a 1D bilateral interpolation of $\frac{V_p}{V_s}$ ratio [24] (Table 1).

4.3. 2004 M_w 6.1 Parkfield Simulation Analyses

In this section, the results of simulation analyses are presented with the purpose of studying the effect of changing the element size and interpolation order on the simulation. To assess the effect of interpolation order, two sets of simulation were performed for constant (P = 0) and linear (P = 1) elements. Considering the constant elements, two simulation analyses were performed using different element sizes. In the first analysis, the fault surface was discretized into 21×9 subfaults. The element size at each subfault is defined to be 1900×1700 m in the directions of strike and dip angles respectively. Furthermore, the fault surface was reproduced and divided into coarser subfaults with the size of 5700 × 5100 m in strike and dip directions respectively. Using the linear interpolation function, various cases of simulations were considered to examine the influence of different parameters. The first parameter is the size of elements. The limiting factor in selecting the size of subfaults is the size that Custodio [12] considered for inversion analyses. Therefore, two element sizes of 1900 × 1700 m and 5700 × 5100 m are considered in strike and dip angles respectively in analogy with analysis cases with constant element. Moreover, each element could be further discretized for calculation of Green's functions and performing the surface integration of Equation (3). Figure (7) depicts different configuration of Green's function and integration points. Table (2) also represents details of each simulation case.

Table 1. Parkfield velocity structure used in the computation of Green's functions [24, 28].

Thickness (m)	Vp (m/s)	Vs (m/s)	Density (kg/m^3)	Qp	Qs
1000	1900	1000	2000	70	35
1000	3400	1700	2300	270	160
1000	4600	2400	2300	450	260
1000	5100	3100	2700	500	300
1400	5600	3600	2700	550	350
13300	6300	3600	2800	600	350
20000	6800	3600	2800	680	360

The goodness-of-fit (GOF) values, as the measures of comparison, are presented in Table (2). As it is clear from this table, by decreasing the size of subfaults, the GOF values are increasing. However, for constant elements (P = 0), there is a pronounced increase in the GOF value when the element size is decreased. Considering the results of linear elements (P = 1), it is possible to observe a kind of trade-off between the element size and number of Green's function inside each subfault.

However, the influence of element size is more effective by comparing simulation cases 3 and 4 in Table (2). In simulation case 3, the subfault size is 5700 × 5100 m in the direction of strike and dip angle respectively, with 16 Green's function elements and nine integration points (Figure 2). Although the distance between Green's points are smaller in case 3, the GOF values of case 4, with more subfaults and less Green's points is higher. This can be associated to the size of asperities as depicted on Figure (6). The size of subfaults shall be small enough to capture the variability of slip on the fault surface, especially at the locations of asperities.

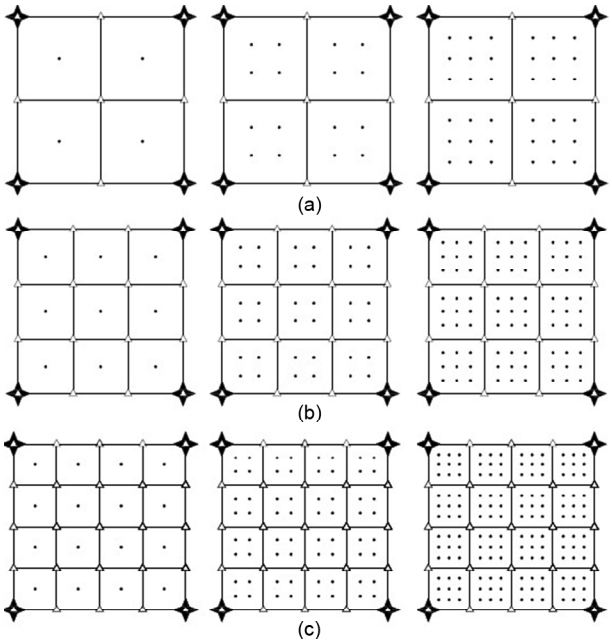

Figure 7. Each subfault is divided into elements depicting a finer grid spacing for Green's functions computations. The elements contain 1, 4 and 9 integration points from left to right, respectively. In subfigure (a) the subfault is divided into four elements, in subfigure (b) into nine elements and in subfigure (c) into 16 elements respectively.

Simulation cases 4-15 represent the effects of considering different numbers of Green's and integration points inside each subfault. As it is clear, increasing the number of Green's and integration points, while the size of the subfaults is fixed to 1900 × 1700 m, will not change the value of GOF considerably. For instance, in EW direction, the GOF values ranges from 4.67 to 4.84, which is approximately 4% of variability. However this is not the case from computational point of view, where, the computation cost of analysis increase considerably by increasing number of Green's points inside each subfault. Comparing simulation case 4 and 15, the number of Green's elements in the latter case is 16 times and the number of integration points is nine times larger than simulation 4. However, the GOF value shows an increase of around 4%. It should be noted that the most intensive and computation consuming part of finite fault modeling is the calculation of Green's functions. However, the results of Table (2) shows that the quality of simulation will not increase considerably

Table 2. Goodness-of-fit verbal value comparison on EW, NS, UP components.

	Sim. No.	N_s^e	N_d^e	d_s^e (m)	d_d^e (m)	N_s^g	N_d^g	$N\xi$	$N\eta$	GOF^{EW}	GOF^{NS}	GOF^{UP}
	1	7	3	5700	5100					1.22	1.15	1.43
P = 0	2	21	9	1900	1700					3.02	3.22	2.15
	3	7	3	5700	5100	4	4	3	3	3.97	3.76	3.24
	4	21	9	1900	1700	1	1	1	1	4.70	4.65	4.60
	5	21	9	1900	1700	1	1	2	2	4.67	4.61	4.50
	6	21	9	1900	1700	1	1	3	3	4.68	4.62	4.54
P – 1	7	21	9	1900	1700	2	2	1	1	4.80	4.67	4.46
	8	21	9	1900	1700	2	2	2	2	4.78	4.67	4.47
	9	21	9	1900	1700	2	2	3	3	4.78	4.68	4.48
	10	21	9	1900	1700	3	3	1	1	4.85	4.69	4.47
	11	21	9	1900	1700	3	3	2	2	4.83	4.69	4.48
	12	21	9	1900	1700	3	3	3	3	4.84	4.69	4.47
	13	21	9	1900	1700	4	4	1	1	4.83	4.68	4.49
	14	21	9	1900	1700	4	4	2	2	4.83	4.69	4.49
	15	21	9	1900	1700	4	4	3	3	4.84	4.69	4.49

N_s^e, N_d^e: The number of subfaults along the strike and dip of the fault respectively.
d_s^e, d_d^e: The size of the subfaults along the strike and dip of the fault respectively.
N_s^g, N_d^g: The number of elements at each subfault used for Green's function calculation along the strike and dip of the fault respectively.
$N\xi$, $N\eta$: The number of integration points in each element along the strike and dip of the fault respectively.
GOF^{EW}, GOF^{NS}, GOF^{UP}: Average of goodness-of-fit verbal values among 26 stations along EW, NS, UP components respectively.

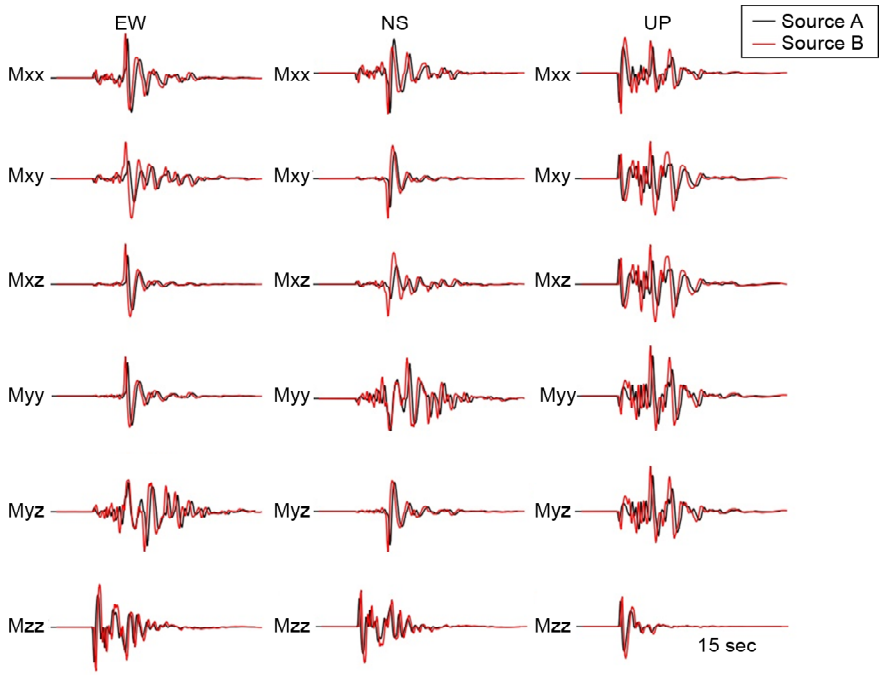

Figure 8. Velocity waveforms of moment tensor elements extracted by forward modeling for CH1E station. The left handed Figures correspond to the EW component, the middle ones belong to the NS component and the right ones to the UP component.

by increasing the number of Green's points inside each subfault.

Having a better understanding of influence of Green's function variability on the results of simulation, Figure (8) depicts a comparison between velocity waveforms of Green's functions moment tensor elements for two point sources A and B. The A and B sources are located at a same layer inside a specific subfault as shown on Figure (9). The waveforms in Figure (8) are shifted to better reveal the similarity of signals. As it is clear from this Figure, six moment tensor elements of Green's function are very similar to each other, suggesting the validity of the assumption of having constant Green's function, with only time shifting according to rupture time, among each subfault, as proposed by [11].

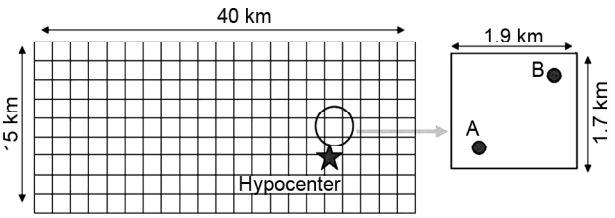

Figure 9. Velocity waveforms of moment tensor elements extracted by forward modeling for CH1E station. The left handed Figures correspond to the EW component, the middle ones belong to the NS component and the right ones to the UP component.

5. Conclusions

The scheme of parameterization and discretization of fault surface has an important effect on the results of finite fault simulation. There are two general techniques for discretizing fault surface, namely, using finer mesh size or increasing order of interpolation. In this paper, both techniques have been examined through simulating a well-known and documented earthquake, the 2004 M_w 6.1 Parkfield. The results of different simulation analyses turns out that both techniques have remarkable influence in increasing the quality of simulation; however, the effect of using finer elements is more pronounced. Considering the distribution of Green's and integration points among each subfault, if the size of the subfault is small enough, in comparison with the size of asperities and the resolution of velocity model of the medium, it is a valid assumption to consider a constant Green's function for each subfault and only apply a time shifting correspond to the arrival time of the rupture. This would be an important result taking into account a large computational demand of calculating Green's function in finite fault inversion and forward modelings.

Acknowledgements

The authors thank the strong motion data center of CESMD [29] for the free internet access of

accelerograms. The authors should also acknowledge source inversion validation (SIV) and the eQuake-RC [30] website, which provides a platform of validated source models. We also should regard late Prof. Hossein Hamzehloo, the former Professor of International Institute of Earthquake Engineering and Seismology which initiated the spadework of this research.

References

1. Udias, A. (1999) *Principle of Seismology*. Cambridge University Press.

2. Hartzell, S. (1978) Earthquake aftershocks as greens functions. Geophys. Res. Lett., 5, 1-4.

3. Irikura, K. (1978) Semi-empirical estimation of strong ground motions during large earthquakes. B*ull. Disast. Prev. Res. Inst.*, Kyoto Univ., **33**, 63-104.

4. Boore, D. (1983) Stochastic simulation of high-frequency ground motions based on seismological models of the radiated spectra. *Bulletin of the Seismological Society of America*, **73**, 1865-1894.

5. Zeng, Y., Anderson, J.G., and Yu, G. (1994) A composite source model for computing realistic synthetic strong ground motions. *Geophys. Res. Lett.*, **21**, 725-728.

6. Hartzell, S., Harmsen, S., and Frankel, S.L. (1999) Calculation of broadband time histories of ground motion: Comparison of methods and validation using strong-ground motion from the 1994 Northridge earthquake. *Bull. Seismol. Soc. Am.*, **89**, 1484-1504.

7. Aki, K. and Richards, P.G. (2002) *Quantitative Seismology*. 2nd Ed. University Science Books.

8. Liu, P. and Archuleta, R.J. (2004) A new nonlinear finite fault inversion with three-dimensional Green's functions: application to the 1989 Loma Prieta, California, earthquake. *J. Geophys. Res.*, 109. DOI 10.1029/2003JB002625.

9. Custodio, S. (2007) *Earthquake Rupture and Ground-Motions: The 2004 Mw 6 Parkfield Earthquake*. Ph.D. Thesis, University of California, Santa Barbara.

10. Hutton, J. (2004) *Fundamental of Finite Analysis, Chap. 6: Interpolation Functions for General Element Formulation*. University Science Books.

11. Olson, A. and Apsel, R. (1982) Finite faults and inverse theory with applications to the 1979 Imperial Valley earthquake. *Bulletin of the Seismological Society of America*, **72**(6), 1969-2001.

12. Custodio, S., Liu, P., and Archuleta, R. (2005) The 2004 M_w 6.0 Parkfield, California, earthquake: Inversion of near-source ground motion using multiple data sets. *Geophys. Res. Lett.*, **32**, 23312.

13. Babuska, I. and Manil, S. (1994) The p and h-p version of the finite element method, basic principles and properties. *Society for Industrial and Applied Mathematics*, **36**, 578-632.

14. Babuska, I. and Manil, S. (1987) The h-p version on finite element method with quasiuniform meshes. *Mathematical Modeling and Numerical Analysis*, **21**, 199-238.

15. Kristekova, M., Kristek, P., and Day, S. (2006) Misfit criteria for quantitative comparison of seismograms. *Bulletin of the Seismological Society of America*, **96**, 1836-1850.

16. Kristekova, M., Kristek, J., and Moczo, P. (2009) Time-frequency misfit and goodness-of-fit criteria for quantitative comparison of signals. *Geophys. J. Int.*, **178**, 813-825.

17. Anderson, J.G. (2004) Quantitative measure of the goodness-of-fit of synthetic seismograms. *13th World Conference on Earthquake Engineering*, Vancouver, B.C., Canada.

18. Ji, C. (2004) Slip history the 2004 (M_w 5.9) Parkfield Earthquake (Single-Plane Model), Caltech, Parkfield 2004, California.

19. Dreger, D.S., Gee, L., Lomband, P., Murray, M.H., and Romanowicz, B. (2005) Strong ground motions : Application to the 2003 M_w 6.5 San Simeon and 2004 M_w 6 Parkfield earthquakes. *Seismo. Res. Lett.*, **76**.

20. Johanson, I.A., Fielding, E.J., Rolandone, F., and

Burgmann, R. (2006) Coseismic and Postseismic slip of the 2004 Parkfiled earthquake from space-geodetic data. *Bull. Seismo, Soc. Am.*, **96**, S269-S282.

21. Mendoza, C. and Hartzell, S., (2004) Finite-fault analysis of the 2004 Parkfield, California earthquake using Pnl waveforms. *Bull. Seismo. Soc. Am.*, **98**, 2746-2755.

22. Barnhart, W.D. and Lohman, R.B. (2010) Automated fault model discretization for inversions for coseismic slip distribution. *Journal of Geophys. Res.*, **115**, DOI:10.1029/2010JB007545.

23. Houlie, N., Dreger, D., and Kim, A. (2014) *GPS Source Solution of the 2004 Parkfield Earthquak*e. Nature-Scientific Reports.

24. Thurber, C., Zhang, H., Waldhauser, F., Hardebeck, J., Michael, A., and Eberhat-Phillips, D. (2006) Three-dimensional compressional wavespeed model, earthquake relocations, and focal mechanisms for the Parkfield, California, region. *Bulletin of the Seismological Society of America*, 38-49.

25. Coutant, O. (1989) *Programme De Simulation Numerique Axitr*a. Grenoble: Res. Report LGIT.

26. Cotton, F. and Coutant O. (1997) Dynamic stress variations due to shear faults in a plane-layered medium. *Geophys. J. Int.*, **128**, 676-688.

27. Bouchon, M. (1981) A simple method to calculate Green's functions for elastic layered media. *Bulletin of the Seismological Society of America*, **71**, 959-971.

28. Thurber, C., Roecker, S., Roberts, K., Gold, M., Powell, L., and Rittger, K. (2003) Earthquake locations and three-dimensional fault zone structure along the creeping station of the san andreas fault near Parkfield. *Geophys. Res. Lett.*, 1112 .

29. CESMD [Online]. Available https://www.strongmotioncenter.org [2016, March].

30. eEQuake-RC [Online] Available http://equake-rc.info/srcmod [2016, March].